OPEN

Evaluating the thermal damage resistance of graphene/carbon nanotube hybrid composite coatings

L. David[1]*, A. Feldman[2]*, E. Mansfield[2], J. Lehman[2] & G. Singh[1]

[1]Mechanical and Nuclear Engineering, Kansas State University Manhattan, Kansas 66506, USA, [2]National Institute of Standards and Technology (NIST) Boulder, Colorado 80305, USA.

We study laser irradiation behavior of multiwalled carbon nanotubes (MWCNT) and chemically modified graphene (rGO)-composite spray coatings for use as a thermal absorber material for high-power laser calorimeters. Spray coatings on aluminum test coupon were exposed to increasing laser irradiance for extended exposure times to quantify their damage threshold and optical absorbance. The coatings, prepared at varying mass % of MWCNTs in rGO, demonstrated significantly higher damage threshold values at 2.5 kW laser power at 10.6 μm wavelength than carbon paint or MWCNTs alone. Electron microscopy and Raman spectroscopy of irradiated specimens show that the coating prepared at 50% CNT loading endure at least 2 kW.cm^{-2} for 10 seconds without significant damage. The improved damage resistance is attributed to the unique structure of the composite in which the MWCNTs act as an efficient absorber of laser light while the much larger rGO sheets surrounding them, dissipate the heat over a wider area.

High-energy lasers are commonly used in optical lithography, laser welding and cutting, and laser surgery. In all of these applications, an accurate calibration of the incident irradiation is necessary for success. Calorimetric methods are commonly used for laser-power calibrations[1]. Here, calorimetry refers to the thermal signal measurements resulting from the conversion of the incident laser energy into heat. High power lasers present significant measurement challenges. To avoid these problems, the National Institute of Standards and Technology (NIST) has been developing a flowing water optical power meter (FWOPM) based on measuring the temperature increase of a water-cooled device.

The present design is a copper cavity that has a black coating on the inside, which captures the laser output and converts it to heat. The cavity is cooled with water flowing through a channel on the outer surface of the copper cone. The chief limitations of the painted copper cavity are damage susceptibility and low thermal transfer to the cooling water. Designing a material that can absorb all of the laser beam's power proves to be a challenge as these lasers are intended to significantly alter their targets.

So far, several coating materials like carbon black, metal black (like aluminum, gold, silver and platinum) have been studied[2-7]. They show good absorbance over a broad wavelength range with low thermal mass. But the primary limitations of these coatings are poor laser-damage threshold and low thermal conductivity[8]. Carbon nanotubes (CNTs) have proven to be a good alternative because of their properties such as high thermal conductivity, high mechanical strength and flat spectral response over a wide wavelength range[8-24]. However, Multi-walled carbon nanotube (MWCNT)-based coatings suffer from severe damage or burn at power densities of approx. 1 kW.cm^{-2} at 10.6 μm exposure[15,16].

A combination of MWCNTs (high optical absorbance and thermal conductivity) and graphene (high in-plane thermal conductivity) could yield an advanced coating material that can absorb laser light over a broad range of wavelength and yet offer improved damage resistance compared to MWCNTs alone, thanks to the exceptional thermal conductivity (approx. 2000 to 4000 W.m^{-1}K^{-1}) and 2-D nature of graphene that can allow uniform spreading of the heat over a relatively large area and to the substrate underneath[25-31]. To this end, we study the synthesis and laser damage tolerance of a novel hybrid composite coating material composed of MWCNTs and chemically-modified graphene (or reduced graphene oxide, rGO). The thermal damage resistance of the hybrid material was tested by preparing dispersion at varying percentages of MWCNTs in GO and then spray coating them on aluminum test coupons used as a representation of the larger thermal-detector surface. The coatings were then exposed to increasing laser irradiance at 10.6 μm, 2.5 kW CO$_2$ laser for extended exposure times.

Integrity of the coating was then studied by observing the morphological and structural changes by means of electron microscopy and Raman spectroscopy.

Experimental procedure

Preparation of graphene oxide. The modified Hummer's method[31] was used to make graphene oxide (GO) with a concentrated solution of H_2SO_4 (130 mL) added to a mixture of graphite flakes (3 g) and $NaNO_3$ (1.5 g). The mixture was cooled using an ice bath. $KMnO_4$ was added slowly to this mixture. The mixture was stirred for 12 hours at 50°C. Then it was quenched with water (400 mL) and 30% H_2O_2 (3 mL) while submerged in an ice bath such that the temperature did not exceed 20°C. The remaining material was then washed with 200 mL of water twice, 200 mL of 30% HCl and 200 mL of ethanol in succession. The material remaining after these extended washes was coagulated with 200 mL of ether and filtered through a paper filter. The filtrate was dried overnight to obtain dry GO.

Composite material and coating preparation. Coating materials was prepared by adding varying mass % of commercially obtained MWCNTs (Bayer Material Science, purity ≥95%), previously deagglomerated by sodium dodecyl benzene sulfonic acid and as-synthesized GO in 50 mL of DI water, followed by sonication for 30 min. These dispersions were then sprayed on to an aluminum test coupon by use of an airbrush at 15 psi of nitrogen gas. The spraying was done with longitudinal passes (with a single pass lasting for approx. 5 s followed by a 10 s pause) while the substrate surface temperature was raised to approx. (80 to 120)°C. Frequent stops between the passes allowed the solvent to evaporate and form a uniform coating. The spraying process was carried out until a visually black coating was realized having an approximate thickness of 10 μm. Four different mass percentages (10, 25, 50 and 75%) of MWCNT in GO, were coated onto four quadrants of a circular aluminum coupon. The samples were then baked overnight at approx. (250 to 300)°C to thermally reduce GO to reduced-graphene oxide (rGO).

Experimental setup. *Laser irradiation.* The coated test specimens were used for studying thermal damage threshold at a wavelength of 10.6 μm produced by a CO_2 (average power 2.5 kW) laser at increasing power densities of 0.5, 2 and approx. 12 kW.cm^{-2}. Details on the laser experimental set-up are available in our previous work[16]. Typically, a laser thermal detector test setup has a flowing-water jacket to absorb the heat transferred from the laser to the copper substrate via the coating material. This flowing water also acts as a sink for the heat transferred. This set-up is rather complex and is not feasible for small-scale damage-threshold testing; hence we utilized an aluminum disk with large mass (to act as a heat sink) as a representation of the calorimeter cone surface.

Thermogravimetric analysis. TGA analysis was performed by use Netzsch Libra thermogravimetric instrument. The instrument was calibrated for 10°C.min^{-1} heating rates using 6 metal samples prior to CNT/GO composite analysis. Samples were heated in a 100 μL alumina pan at a rate of 10°C.min^{-1} to 1000°C after a brief equilibration step at 40°C. Air was introduced at a rate of 25 mL.min^{-1} during sample analysis, with 20 mL.min^{-1} of nitrogen protective gas.

X-ray diffraction (XRD). XRD was performed by Bruker powder X-ray diffractometer operating at room temperature, with Cu Kα radiation and nickel filter.

Scanning electron microscopy. SEM analysis of the coatings was done by use of a Carl Zeiss EVO low-vacuum SEM operating at 5 kV with 25 mm (low resolution) and 10 mm (high resolution) working distance.

Reflectance measurements. Hemispherical reflectance measurements (350 nm to 2500 nm) were performed using a Perkin Elmer Lambda 1050 compared to a NIST traceable black spectralon reference material.

Raman spectroscopy. Raman spectra were collected with a HORIBA LabRAM ARMIS spectrometer using a 17 mW HeNe laser source (632.8 nm wavelength (1.96 eV)). The spectra were collected using a
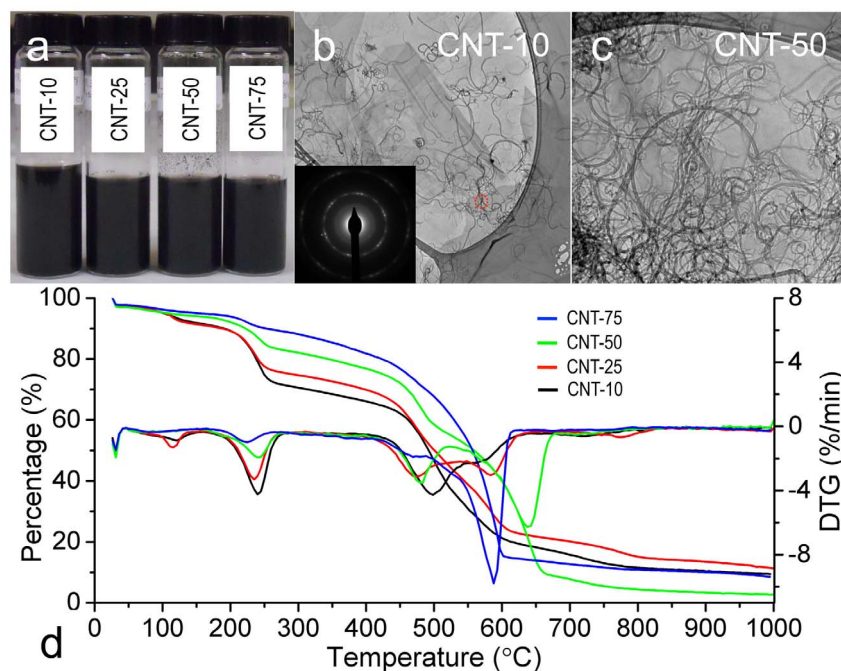

Figure 1 | (a) Digital image of various CNT/GO dispersions, kept stable for 48 h. TEM image of CNT/GO composite mix at (b) 10% and (c) 50% CNT loadings. The scale bar is 100 nm. (d) Thermogram and first derivative with respect to temperature of CNT/GO samples. Blue = 75% CNT in GO; Green = 50% CNT in GO; Red = 25% CNT in GO; Black = 10% CNT in GO.

100 × NIR objective lens (theoretical spot size: 842 nm), 200 μm confocal hole, 150 μm wide entrance slit, 600 gr.mm^{-1} grating.

Disclaimer. Commercial equipment, instruments, or materials are identified only in order to adequately specify certain procedures. In no case does such identification imply recommendation or endorsement by the National Institute of Standards and Technology (NIST), nor does it imply that the products identified are necessarily the best available for the purpose. U.S. Government work not protected by U.S. copyright.

Results and Discussion

As seen in Fig. 1a, the surfactant functionalized CNTs/GO dispersions were observed to be uniform and generally stable in water for days. Although any sort of chemical functionalization of CNTs and/or graphene is likely to compromise the thermal conductivity of the material[32,33], it generally tends to increase the coupling between CNTs and graphene resulting in homogeneous and stable dispersions (crucial for spray coating)[34–38]. The size and distribution of CNTs and GO sheets was observed in the transmission electron microscope (TEM). Shown in Fig. 1(b and c) are the TEM images of CNT/GO composite with 10% (CNT-10) and 50% CNT (CNT-50) loading, respectively. The insert is the selected area electron diffraction pattern (SAED) of the spot marked with a red circle in the corresponding TEM image that shows a typical ring pattern that is characteristic of CNTs. The tubes were observed to be approx. 13 nm in (average) diameter and approx. (0.5 to 3) μm in length, clearly seen as being sandwiched or supported by the large area (approx. 5 μm × 1 μm or larger in size) GO sheets. No large CNT bundles or agglomeration was evident, further suggesting uniform mixing of CNTs in the GO matrix.

Later, TGA analysis of the composite dispersions was performed, which is presented in Fig. 1(d). For all compositions, four transitions were typically observed. A small peak centered around (100 to 120)°C, was most likely the loss of associated water. Second, a peak centered around 240°C. This peak is significant in the low CNT % samples, which indicates it may be due to removal of labile oxygen groups in GO[39]. A third peak centered around 480°C and 595°C are due to the presence of MWCNTs in the sample. From previous work, it has been shown that MWCNTs (from the same batch) can have oxidation temperature approx. 530 to 610°C[40,41]. The low temperature peak around 480°C decreases in size with increasing CNT content. This peak could be due to the formation of some sort of GO-CNT mixed complex. With increasing MWCNT content, the percentage of this complex in the sample decreases with respect to the MWCNT content. Lastly, the peak at 595°C is attributed to the presence of MWCNTs alone.

The laser damage evolution of the coatings was analyzed and compared by use of digital camera imaging, SEM and Raman spectroscopy. Prior to the irradiation tests, thermal reduction of the CNT/GO composite coating to CNT/rGO composite was confirmed by X-ray diffraction analysis shown in Fig. 2(a). Figure 2 (b, c) shows a schematic and optical image of the aluminum coupon that marks the locations at which the coatings were irradiated. To independently sample multiple exposures, we rotated the coupon clockwise with respect to the incoming laser light, with the lowest irradiance at a lesser angle, the medium at the maximum angle of the quadrant, and the highest power closer to the center. An optical photograph of the coated Al coupon after laser irradiation testing is shown in Fig. 2(c). It can be clearly seen that the irradiance of 0.5 kW.cm^{-2} for 10 s, did not leave a visible mark on any of the coatings. This was not surprising since the MWCNT coatings have been shown to resist damage up to 1 kW.cm^{-2} at 10.6 μm exposure[16]. The SEM and Raman data corresponding to 0.5 kW.cm^{-2} irradiance is, therefore presented as Supplementary Fig. S1, and S2. However, irradiance at 2 and 12 kW.cm^{-2} left a prominent mark on most of the coatings. The visual damage due to 12 kW.cm^{-2} irradiance was observed to be higher for 75% of CNT loading (CNT-75 quadrant). This was further supported by the digital camera videography in which CNT-75 could be seen as undergoing continued sparking (or flashes of light emerging from irradiation) throughout the 10 s irradiation period (Supplementary Media File S1), while specimen at 50% loading appeared to be largely stable toward irradiation (Supplementary Media File S2). Another important observation was the blinding
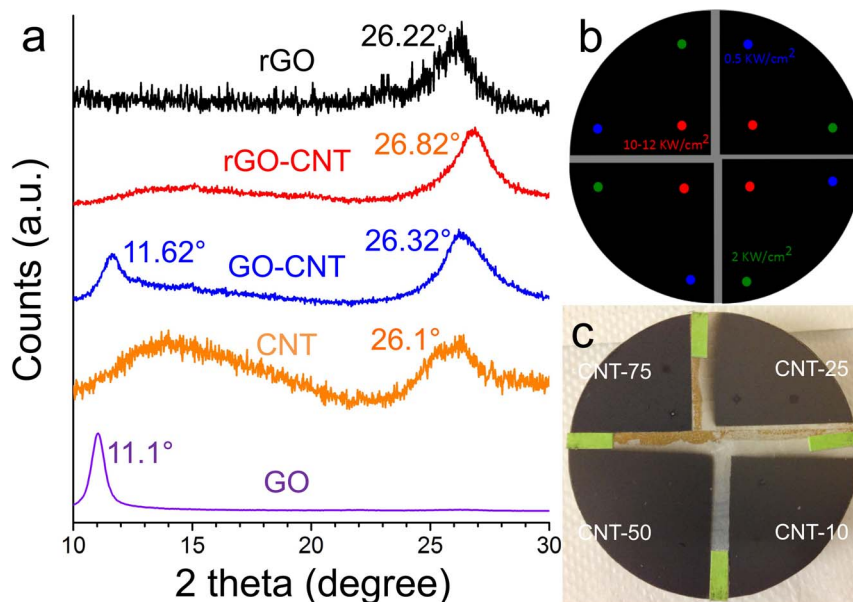

Figure 2 | (a) X-ray diffraction data confirming thermal reduction of GO to rGO in the composite coating. Data for as-received MWCNTs, as-prepared GO, and rGO specimens is included for comparison purposes. (b) Schematic showing the location of various spots that were laser irradiated at 0.5, 2 and 12 kW.cm^{-2} power densities for 10 s. (c) Post irradiation optical photograph of aluminum coupon coated with composite material with different concentration of CNTs in each quadrant. Note that the irradiance at 0.5 kW.cm^{-2} did not leave a visible mark on any of the coatings while 2 and 12 kW.cm^{-2} irradiance left a prominent mark on most of the coatings. The visual damage due to 12 kW.cm^{-2} irradiance was observed to increase with increasing percentage of CNTs.

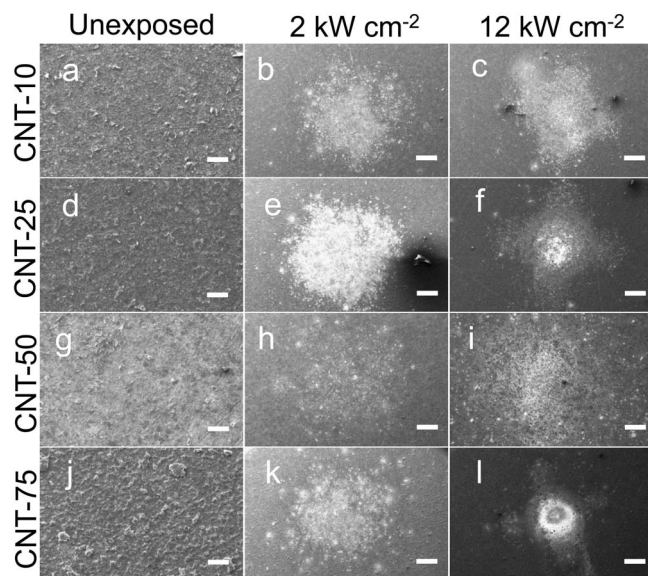**Figure 3 | Low-resolution SEM images of composite coatings with 10, 25, 50 and 75% CNTs irradiated with a laser having 0 (unexposed), 2 and 12 kW.cm⁻² power densities.** The scale bar is 100 μm.

bright glow (pause at t = 3 to 4 s) from the coating surface as the laser light made its the first contact with the specimen surface, most likely due to black body radiation at high temperatures. The intensity of this glow (or reflection of laser light) was observed to be higher for CNT-10 and CNT-25 coatings than CNT-50 (Supplementary Media Files S3 and S4, respectively).

A more detailed analysis of the structural morphology, both before and after irradiation was studied by use of SEM. Figure 3 and 4 are the low and high magnification SEM micrographs that show the effect of incremental laser irradiation on the coatings. At low magnifications, the non-irradiated surface exhibited a robust and visually uniform coating. As the laser irradiance was increased, a noticeable change was observed on the coating surface. With 2 kW.cm⁻² exposure, the areas irradiated by the laser appeared brighter (mostly likely SEM image charging), whereas the unexposed areas were still relatively dark. High magnification images obtained from the same area
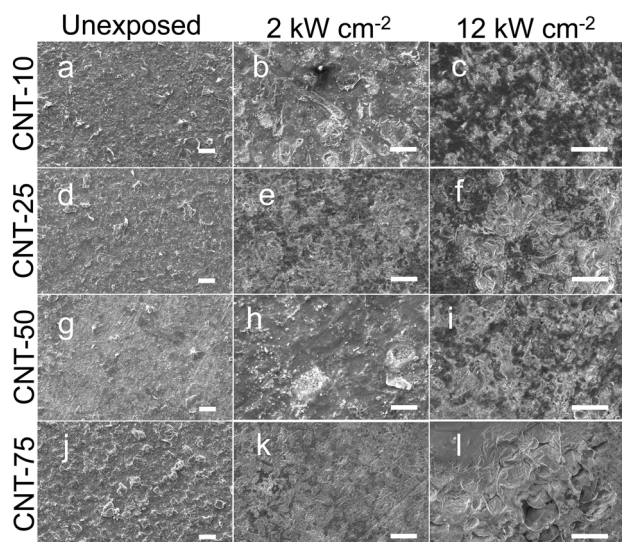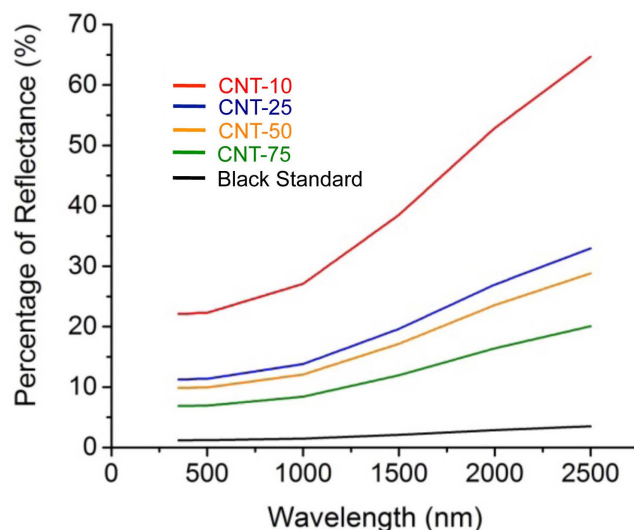

Figure 5 | Hemispherical reflectance measurements, that compares the reflectance of CNT/rGO material to a NIST-traceable black reference material over a wide wavelength range.

showed no significant change in morphology when compare to that from the non-irradiated spots. This observation suggests partial oxidation of the top layer in the coating, which was visible only at lower magnifications. On further increasing of laser power density to approx. 12 kW.cm⁻², damage to the coating was evident, especially in the case of CNT-75 coating. This was further confirmed by the presence of carbon clusters in the high magnification images of the same area. A comparison of CNT-50 and CNT-75 low magnification images (Fig. 3i and l) suggests that the heat flux was concentrated to a smaller region in case of CNT-75, while the spread was more uniform in case of specimen with high rGO concentrations i.e., CNT-50.

Further, ex-situ measurements were performed to compare the optical response from the four different coating areas, which is presented in Fig. 5. It is clear that specimens with higher rGO percentage were more reflecting, particularly at increasing wavelengths. This could be attributed to the presence of carboxy, epoxy, alkoxy carbons and perhaps trace metallic impurities that are present in rGO (prepared by modified Hummer's method) even after thermal reduc-
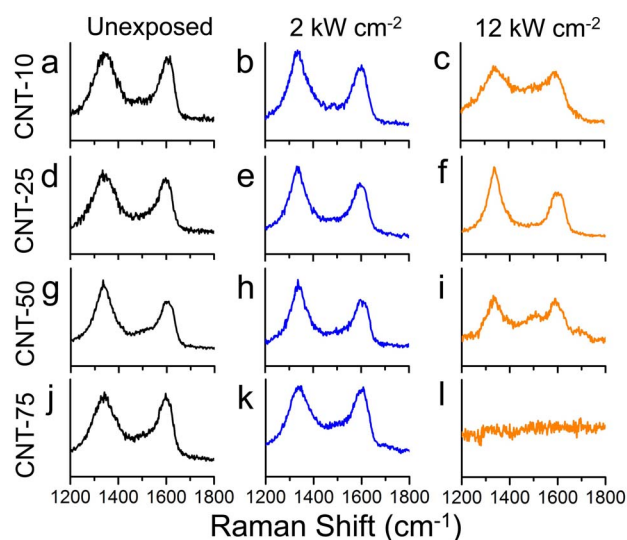

Figure 4 | High-resolution SEM images of composite coatings with varying CNT loading, irradiated at 0 (unexposed), 2 and 12 kW.cm⁻² power densities. The scale bar is 40 μm.

Figure 6 | Raman spectra of composite coatings with 10, 25, 50 and 75% CNTs irradiated at 0 (unexposed), 2 and 12 kW.cm⁻² power densities.

Table 1 | Dependence of I_D and I_D/I_G as observed in the Raman spectra, on the incident laser irradiation power density

Specimen		Irradiance, KW. cm^{-2}			
		0	0.5	2	12
CNT-10	I_D/I_G	1.04	1.09	1.13	1.12
	FWHM D-Peak, cm^{-1}	94.31	83.53	93.46	68.49
	FWHM G-Peak, cm^{-1}	60.62	60.18	62.16	60.89
CNT-25	I_D/I_G	1.08	1.16	1.23	1.36
	FWHM D-Peak, cm^{-1}	67.26	76.52	62.42	58.64
	FWHM G-Peak, cm^{-1}	55.09	59.72	62.51	58.58
CNT-50	I_D/I_G	1.11	1.16	1.29	1.33
	FWHM D-Peak, cm^{-1}	74.33	59.5	54.61	59.43
	FWHM G-Peak, cm^{-1}	61.28	61.38	57.31	60.34
CNT-75	I_D/I_G	1.15	1.26	1.37	NA
	FWHM D-Peak, cm^{-1}	67.97	74.23	63.32	NA
	FWHM G-Peak, cm^{-1}	59.67	60.44	58.5	NA

tion[32,39]. The presence of optimum amount of CNTs and complete thermal reduction of GO in the composite is therefore crucial for applications that demand uniform optical absorbance for a broad range of wavelength (UV to far IR).

To further understand the damage observed using SEM, Raman spectroscopy was performed. Raman spectra of carbon-based materials have two distinct peaks. The "G" peak or graphite peak ($\sim$1600 cm^{-1}) is representative of the in-plane vibrational modes of carbon in graphite lattice (sp^2 hybridized carbon) while "D" peak or defect peak ($\sim$1350 cm^{-1}) is generated by the presence of defects in the graphite lattice (-sp^3 hybridized carbon)[43-51]. Fig. 6 shows the Raman spectra for various percentages of CNT-rGO composite coatings exposed to increasing laser power densities. For comparison purposes, the Raman data for as-prepared rGO and CNT powders is included in Supplementary Information Fig. S3.

The ratio of the D-peak to the G-peak (I_D/I_G) was higher for the exposed areas when compared to those of the unexposed areas. Also, the I_D/I_G ratio generally increased with the increasing irradiation power density and then stabilized, see Table 1. This result is representative of changes in the amount of defects and the degree of graphitization of the composite coating. This trend is comparative to the amorphization trajectory proposed by Ferrari and Robertson for carbon materials[42,45]. The initial increase, followed by stabilization in the I_D/I_G ratio suggests the coating to be in phase I and phase II of the trajectory, respectively. These observations are somewhat similar to those made by Balandin's group in their work on electron beam irradiation of mechanically exfoliated graphene specimens[52]. Raman spectrum of CNT-10, CNT-25, and CNT-50 coating exposed to laser irradiation of 12 kW.cm^{-2}, showed clear D and G peak signatures while for the composite coating with 75% CNTs, the spectra were severely distorted, corroborating observations made in SEM and digital micrographs. Overall, the improved laser damage threshold of CNT-10 and CNT-50 specimen can be attributed to graphene's (in the composite) ability to very efficiently dissipate heat across a large area thus preventing the coating from getting damaged.

Conclusion

Overall, for the first time we study the damage incurred by CNT-rGO hybrid composite coatings that were exposed to incremental laser irradiation up to 12 kW.cm^{-2} at 10.6 μm wavelength. Digital camera and SEM images showed no major change in surface morphology at 0.5 and 2 kW.cm^{-2} irradiance, while formation of carbon clusters were clearly evident when the power density was increased to approx. 12 kW.cm^{-2}. These observations were supported by analysis of Raman spectra obtained from the irradiated spots. The Raman I_D/I_G ratio generally increased with increased irradiance implying more damage to the graphitic structure at higher power densities particularly for specimen with CNT loading higher than 50%.

These observations, which depict the structural changes in the CNT-rGO composite upon exposure to extreme heat flux, may have important implications for the design of next generation of optical absorbers and thermal coatings for applications in harsh environments.

1. Gunn, S. R. Calorimetric measurements of laser energy and power. *J. Phys. E Sci. Instrum.* **6**, 105–114 (1973).
2. Advena, D. J., Bly, V. T. & Cox, J. T. Deposition and characterization of far-infrared absorbing gold black films. *Appl. Opt.* **32**, 1136–1144 (1993).
3. Blevin, W. R. & Geist, J. Infrared Reflectometry with a Cavity-Shaped Pyroelectric Detector. *Appl. Opt.* **13**, 2212–2217 (1974).
4. Blevin, W. R. & Geist, J. Influence of Black Coatings on Pyroelectric Detectors. *Appl. Opt.* **13**, 1171–1178 (1974).
5. Lehman, J., Theocharous, E., Eppeldauer, G. & Pannell, C. Gold-black coatings for freestanding pyroelectric detectors. *Meas. Sci. Technol.* **14**, 916–922 (2003).
6. Betts, D. B., Clarke, F. J., Cox, L. J. & Larkin, J. A. Infrared reflection properties of five types of black coating for radiometric detectors. *J. Phys. E Sci. Instrum.* **18**, 689 (1985).
7. Nelms, N. & Dowson, J. Goldblack coating for thermal infrared detectors. *Sensor Actuat. A-Phys.* **120**, 403–407 (2005).
8. Singh, G., Rice, P., Hurst, K. E., Lehman, J. H. & Mahajan, R. L. Laser-induced exfoliation of amorphous carbon layer on an individual multiwall carbon nanotube. *Appl. Phys. Lett.* **91**(3), 033101 (2007).
9. Bhandavat, R., Feldman, A., Cromer, C., Lehman, J. & Singh, G. Very High Laser-Damage Threshold of Polymer-derived Si(B)CN-Carbon Nanotube Composite Coatings. *ACS Appl. Mater. Inter.* **5**, 2354–2359 (2013).
10. Berber, S., Kwon, Y. K. & Tomanek, D. Unusually high thermal conductivity of carbon nanotubes. *Phys. Rev. Lett.* **84**, 4613–4616 (2000).
11. Choi, T. Y., Poulikakos, D., Tharian, J. & Sennhauser, U. Measurement of thermal conductivity of individual multiwalled carbon nanotubes by the 3-omega method. *Appl. Phys. Lett.* **87**(1), 013108 (2005).
12. Yang, D. J. *et al.* Thermal conductivity of multiwalled carbon nanotubes. *Phys. Rev. B* **66**(16), 165440 (2002).
13. Chunnilall, C. J., Lehman, J. H., Theocharous, E. & Sanders, A. Infrared hemispherical reflectance of carbon nanotube mats and arrays in the 5–50 mu m wavelength region. *Carbon* **50**, 5348–5350 (2012).
14. Hurst, K. E., Dillon, A. C., Yang, S. & Lehman, J. H. Purification of Single Wall Carbon Nanotubes As a Function of UV Wavelength, Atmosphere, and Temperature. *J. Phys. Chem. C* **112**, 16296–16300 (2008).
15. Ramadurai, K., Cromer, C. L., Li, X., Mahajan, R. L. & Lehman, J. H. Foam-based optical absorber for high-power laser radiometry. *Appl. Opt.* **46**, 8268–8271 (2007).
16. Ramadurai, K., Cromer, C. L., Dillon, A. C., Mahajan, R. L. & Lehman, J. H. Raman and electron microscopy analysis of carbon nanotubes exposed to high power laser irradiance. *J. Appl. Phys.* **105**(9), 093106 (2009).
17. Ramadurai, K. *et al.* High-performance carbon nanotube coatings for high-power laser radiometry. *J. Appl. Phys.* **103**(1), 013103 (2008).
18. Lehman, J. H., Engtrakul, C., Gennett, T. & Dillon, A. C. Single-wall carbon nanotube coating on a pyroelectric detector. *Appl. Opt.* **44**, 483–488 (2005).
19. Theocharous, E., Deshpande, R., Dillon, A. C. & Lehman, J. Evaluation of a pyroelectric detector with a carbon multiwalled nanotube black coating in the infrared. *Appl. Opt.* **45**, 1093–1097 (2006).
20. Bai, X. D. *et al.* Laser irradiation for purification of aligned carbon nanotube films. *Carbon* **42**, 2125–2127 (2004).
21. Huang, H. J., Maruyama, R., Noda, K., Kajiura, H. & Kadono, K. Preferential destruction of metallic single-walled carbon nanotubes by laser irradiation. *J Phys Chem B* **110**, 7316–7320 (2006).

22. Zhang, Y. *et al.* Structural changes in double-walled carbon nanotube strands induced by ultraviolet laser irradiation. *J. Phys. Chem. C* **111**, 2901–2905 (2007).

23. Hung, W. H., Kumar, R., Bushmaker, A., Cronin, S. B. & Bronikowski, M. J. Rapid prototyping of three-dimensional microstructures from multiwalled carbon nanotubes. *Appl. Phys. Lett.* **91**(9), 093121 (2007).

24. Kichambare, P. D. *et al.* Laser irradiation of carbon nanotubes. *Mater. Chem. Phys.* **72**, 218–222 (2001).

25. Balandin, A. A. Thermal properties of graphene and nanostructured carbon materials. *Nature Mat.* **10**, 569–581 (2011).

26. Pop, E., Varshney, V. & Roy, A. K. Thermal properties of graphene: Fundamentals and applications. *MRS Bull.* **37**, 1273–1281 (2012).

27. Klemens, P. G. & Pedraza, D. F. Thermal conductivity of graphite in basal plane. *Carbon* **32**, 735–741 (1994).

28. Klemens, P. G. Theory of thermal conduction in the ceramic films. *Int. J. Thermophys.* **22**, 265–275 (2001).

29. Nika, D. L., Pokatilov, E. P., Askerov, A. S. & Balandin, A. A. Phonon thermal conduction in graphene: Role of Umklapp and edge roughness scattering. *Phys. Rev.* **79**(15), 155413 (2009).

30. Evans, W. J., Hu, L. & Keblinski, P. Thermal conductivity of graphene ribbons from equilibrium molecular dynamics: Effect of ribbon width, edge roughness, and hydrogen termination. *Appl. Phys. Lett.* **96**(20), 203112 (2010).

31. Lindsay, L., Broido, D. A. & Mingo, N. Flexural phonons and thermal transport in graphene. *Phys. Rev. B* **82**, 115427 (2010).

32. Marcano, D. C. *et al.* Improved synthesis of graphene oxide. *ACS Nano* **4**, 4806–4814 (2010).

33. Gulotty, R., Castellino, M., Jagdale, P., Tagliaferro, A. & Balandin, A. A. Effects of functionalization on thermal properties of single-wall and multi-wall carbon nanotube–polymer nanocomposites. *ACS Nano* **7**, 5114–5121 (2013).

34. Shahil, K. M. F. & Balandin, A. A. Graphene−multilayer graphene nanocomposites as highly efficient thermal interface materials. *Nano Lett.* **12**, 861–867 (2012).

35. Dong, X. *et al.* The formation of a carbon nanotube-graphene oxide core-shell structure and its possible applications. *Carbon* **49**, 5071–5078 (2011).

36. Guo, Z. *et al.* Leaf-like graphene oxide with a carbon nanotube midrib and its application in energy storage devices. *Adv. Funct. Mater.* **23**, 4840–4846 (2013).

37. Jia, Y., Yu, K. & Qian, K. Facile approach to prepare multi-walled carbon nanotubes/graphene nanoplatelets hybrid materials. *Nanoscale Res. Lett.* **8**, 243 (2013).

38. Ma, J. *et al.* Surfactant-free synthesis of graphene-functionalized carbon nanotube film as a catalytic counter electrode in dye-sensitized solar cells. *J. Power Sources* **247**, 999–1004 (2014).

39. Tristan-Lopez, F. *et al.* Large area films of alternating graphene-carbon nanotube layers processed in water. *ACS Nano* **7**, 10788–10798 (2013).

40. Stankovich, S. *et al.* Synthesis of graphene-based nanosheets via chemical reduction of exfoliated graphite oxide. *Carbon* **45**, 1558–1565 (2007).

41. Bhandavat, R., Kuhn, W., Mansfield, E., Lehman, J. & Singh, G. Synthesis of Polymer-Derived Ceramic Si(B)CN-Carbon Nanotube Composite by Microwave-Induced Interfacial Polarization. *ACS- Appl. Mater. Inter.* **4**, 11–16 (2012).

42. Lehman, J. H. *et al.* Core-shell composite of SiCN and multiwalled carbon nanotubes from toluene dispersion. *J. Mater. Sci.* **45**, 4251–4254 (2010).

43. Ferrari, A. C. Raman spectroscopy of graphene and graphite: Disorder, electron-phonon coupling, doping and nonadiabatic effects. *Solid State Commun.* **143**, 47–57 (2007).

44. David, L. *et al.* Synthesis of Graphene Films by Rapid Heating and Quenching at Ambient Pressures and Their Electrochemical Characterization. *ACS- Appl. Mater. Inter.* **5**, 546–552 (2013).

45. Hao, Q. *et al.* Surface-Enhanced Raman Scattering Study on Graphene-Coated Metallic Nanostructure Substrates. *J. Phys. Chem. C* **116**, 7249–7254 (2012).

46. Ferrari, A. C. & Robertson, J. Interpretation of Raman spectra of disordered and amorphous carbon. *Phys. Rev. B* **61**, 14095–14107 (2000).

47. Cuesta, A., Dhamelincourt, P., Laureyns, J., Martinezalonso, A. & Tascon, J. M. D. Raman microprobe studies on carbon materials. *Carbon* **32**, 1523–1532 (1994).

48. Bacsa, W. S., Deheer, W. A., Ugarte, D. & Chatelain, A. Raman spectroscopy of closed-shell carbon particles. *Chem. Phys. Lett.* **211**, 346–352 (1993).

49. Gruber, T., Zerda, T. W. & Gerspacher, M. Raman studies of heat-treated carbon blacks. *Carbon* **32**, 1377–1382 (1994).

50. Jawhari, T., Roid, A. & Casado, J. Raman spectroscopic characterization of some commercially available carbon black materials. *Carbon* **33**, 1561–1565 (1995).

51. Ivleva, N. P., Messerer, A., Yang, X., Niessner, R. & Poeschl, U. Raman microspectroscopic analysis of changes in the chemical structure and reactivity of soot in a diesel exhaust after treatment model system. *Environ. Sci. Technol.* **41**, 3702–3707 (2007).

52. Teweldebrhan, D. & Balandin, A. A. Modification of graphene properties due to electron-beam irradiation. *Appl. Phys. Lett.* **94**, 013101 (2009).

Acknowledgments

Author contributions

Additional information